Roadmap for the Design of All Ferromagnetic Four-Terminal Spin Valves and the Extraction of Spin Diffusion Length

E. Fourneau,[1,*] A.V. Silhanek,[2] and N.D. Nguyen[1]

[1]*Solid-State Physics—Interfaces and Nanostructures, Q-MAT, CESAM, University of Liége, 4000 Liége, Belgium*
[2]*Experimental Physics of Nanostructured Materials, Q-MAT, CESAM, University of Liége, 4000 Liége, Belgium*

Graphene is a promising substrate for future spintronic devices owing to its remarkable electronic mobility and low spin-orbit coupling. Hanle precession in spin-valve devices is commonly used to evaluate spin diffusion and spin lifetime. In this work, we demonstrate that this method is no longer accurate when the distance between the inner and outer electrodes is smaller than 6 times the spin diffusion length, leading to errors as large as 50% for the calculation of the spin figures of merit of graphene-based devices. We suggest simple but efficient approaches to circumvent this limitation by addressing a revised version of the Hanle fit function. Complementarily, we provide clear guidelines for the design of four-terminal nonlocal spin valves suitable for the flawless determination of the spin lifetime and the spin diffusion coefficient.

I. INTRODUCTION

The emergence of two-dimensional materials offers alternative paths for the development of spintronic devices due to their high carrier mobility and low spin-orbit coupling [1,2]. In graphene, coherent spin transport of tens of micrometers has been reported [3–6]. Currently, efforts are still ongoing to improve the material quality and understand the underlying mechanisms responsible for the spin-relaxation phenomenon. Such efforts aim at closing the gap between experimental observations and the theoretical expectation of a 100-μm spin diffusion length [2,7–9].

Hanle spin-precession experiments performed in a four-terminal nonlocal-spin-valve (NLSV) geometry (see Fig. 1) provide an elegant method to evaluate the spin-transport properties of a material. In such a device, a current is applied between a ferromagnetic (FM) injector (electrode E_2) and the reference electrode (E_1). Consequently, a spin current is generated under those electrodes that also diffuses toward the detection electrode (E_3 or E_3'). Therefore, an electric voltage proportional to the spin accumulation (μ_s) under the detection electrode is probed with respect to the reference electrode (E_4). This electrical potential difference $V_a = V(E_3) - V(E_4)$ is called the "spin voltage." In Hanle experiments, the change of spin voltage as a function of the intensity of a perpendicular magnetic field ($B_\perp$), which induces precession of spin carriers, is measured. Routinely, experimental results are fitted with the solution of the modified Bloch equations describing diffusive transport in the presence of spin precession, naturally leading to two figures of merit (FOMs) of the spin transport: the spin lifetime τ_{sf} and the spin diffusion coefficient D_s [10,11]. However, this approach is limited by the following hypotheses:

(a) No spin absorption (contact-induced spin relaxation) at any of the contact electrodes
(b) A one-dimensional infinite diffusive medium
(c) An infinite distance between the inner (E_2, E_3) and outer (E_1, E_4) electrodes
(d) Zero-width electrodes
(e) Nonmagnetic (NM) outer electrodes

The contact-induced spin relaxation has been widely investigated [12–17], and various models that include the presence of low-resistance injector or detector contacts, as well as the presence of a bias applied to the detector, have been developed [18–21]. However, limited theoretical efforts have been devoted so far to understand the effect of geometry despite the large variety of designs and layouts implemented in experimental investigations. With a finite diffusive medium, specular reflection is expected at transport-material edges, leading to an increase of the spin signal [22], whereas a short separation between FM inner electrodes and NM outer electrodes induces premature relaxation of spin, leading to a decrease of the global spin lifetime when outer electrodes are transparent [23,24]. In addition, the electrode width can be an important feature when its dimension exceeds several hundred nanometers. Spiesser *et al.* [25,26] showed that a more-accurate theoretical prediction can be obtained by integration over the
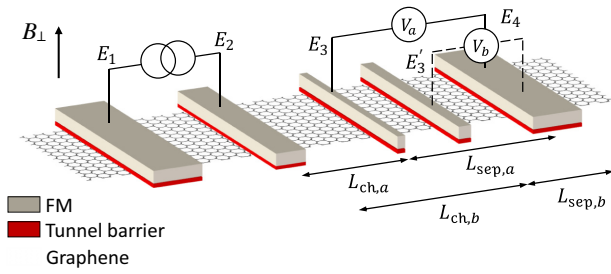
---

*emile.fourneau@uliege.be

FIG. 1.   A typical spin valve with FM contacts, suitable for spin-precession experiments, with different channel lengths (e.g., using electrode E'_3 instead of electrode E_3) in the same graphene sheet. Two measurement configurations are proposed, with different distances between the detector and the outer electrode.
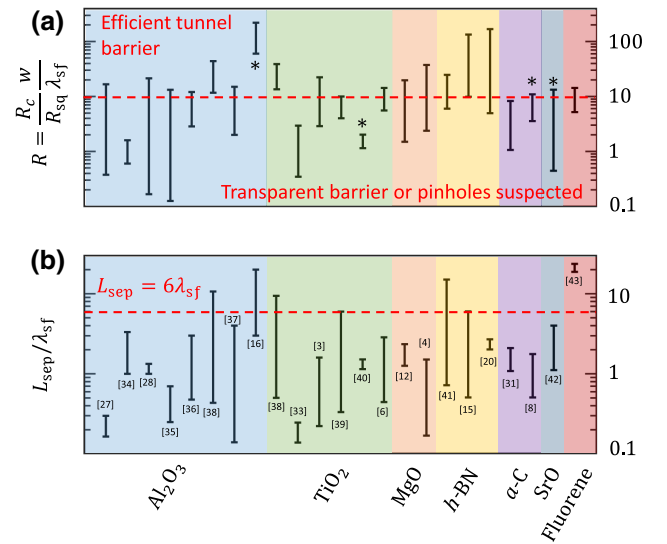

FIG. 2.   Summary of a representative set of graphene-based NLSV experiments reported in the literature (each bar corresponds to a single scientific publication) for which sufficiently accurate information relative to the contact resistance, dimensions, and position is provided. The data range is defined by the highest and lowest values reported in the corresponding paper. For each barrier material, results are sorted chronologically: Al_2O_3 [16,27,28,34–38]; TiO_2 [3,6,33,38–40]; MgO [4,12]; hexagonal BN (h-BN) [15,20,41]; amorphous C (a-C) [8,31]; SrO [42]; fluorene [43]. (a) Evaluated $R = R_c W / R_{sq} \lambda_{sf}$ for different tunnel-barrier materials. The dashed red line corresponds to the lower limit for high-quality contact suggested in Ref. [16]. (b) Ratio of the measured spin diffusion length versus the distance between the inner and outer detection electrodes. The dashed red line shows the limit of $L_{sep} = 6\lambda_{sf}$, above which a negligible effect of outer electrodes is expected.

injector width. The nonfulfillment of the fifth hypothesis is often observed in spin-valve experiments. In this case, it was shown that the spin-signal intensity depends on the magnetic orientation of both inner and outer electrodes [27–32]. However, quite surprisingly, there is no general study of its impact on the extracted spin-transport FOMs in Hanle precession experiments. Only the case of graphene nanoislands smaller than 1 μm was analyzed [33]. Moreover, no practical solution (neither for an experimental nor a modeling purpose) has been suggested to correctly account for the modification introduced by the presence of FM outer electrodes. Addressing the third hypothesis, one can observe that as long as the spin diffusion length ($\lambda_{sf} = \sqrt{\tau_{sf} D_s}$) is short compared with the distance between the contacts ($L_{sep,b}$ in Fig. 1), the assumption of infinite distances is acceptable since the injected spin signal vanishes before reaching the outer reference electrodes. For higher values of λ_{sf}, a conflict emerges between the simplification or optimization of fabrication processes and the accuracy on the calculated spin FOMs. Indeed, the most-popular method reported in the literature consists in a single lithography step to define multiple contacts followed by the deposition of two successive layers, a tunnel barrier (oxide, hexagonal BN, etc.) and a FM metal. As a consequence, all electrodes can act as a spin injector or detector, with the major benefit of having different channel lengths in a single device depending on the connections chosen. As shown in Fig. 1, there are two options for the device configuration: configuration a, with electrode E_3 and channel length $L_{ch,a}$, and configuration b, with electrode E'_3 and a larger channel length $L_{ch,b}$. However, the distance between inner and outer electrodes varies as well with the selected set of electrodes ($L_{sep,a}$ and $L_{sep,b}$ respectively), leading to different extracted FOMs, as discussed in this work.

In light of the results reported previously in the literature, it appears that great effort has been directed to obtain high-quality tunnel barriers, free of pinholes. Figure 2(a) summarizes a selected set of graphene-based spin-valve experiments for several barrier materials and sorted in

chronological order. It should be noticed that irrespective of the used material, recent publications report progressively higher values of the R parameter, the ratio between contact resistance and channel spin resistance proposed by Popinciuc *et al.* [35], reaching the lower bound of 10 suggested by Stecklein *et al.* [16]. On the other hand, all devices reported in Fig. 2 use FM outer electrodes, except for those with an asterisk [8,16,40,42]. This feature is important because, as shown in Fig. 2(b), nearly all devices have a spin diffusion length on the order of the distance between the inner and outer electrodes, making a comparison between FOMs reported in different papers difficult. Experimentally, the position of the outer electrodes is also critical because a short separation distance L_{sep} greatly improves the Hanle measurement quality as it reduces drastically the experimental noise. The question naturally arises as how to optimally combine competing requirements from theory and experiment.

In this work, the impact of the position and the material of the outer electrodes is clarified via spin-transport simulations in graphene. More importantly, we deduce a series

of criteria that must be fulfilled by nominal spin-valve devices. Moreover, an updated version of the solution of the modified classical fit function derived from the solution of the one-dimensional Bloch equations is proposed to include the effect of the distance between electrodes. Even though this work focuses exclusively on graphene as a diffusive medium, our findings are applicable to any kind of pseudosubstrate with sufficiently-high-quality spin-transport properties.

II. SPIN DRIFT-DIFFUSION AND HANLE CALCULATIONS

To demonstrate the importance of the relative magnetic orientation of the outer contact electrodes, calculations are performed based on data reported in Ref. [6]. Information regarding the calculation details are provided in Appendix A. Solving the spin drift-diffusion equations allows one to obtain the spin-accumulation profile along the device, as shown in Fig. 3(a)for two relative magnetic orientations of the injector (orange and blue curves). We consider first the case where no $B_\perp$ field is applied (solid line). It is worth noting that the model reproduces the diffusive behavior of the spin-injection theory, with an exponential decay depending on the channel properties, leading to no signal far on the right side of the injector (E_2) [44]. On the

other hand, the signal never reaches zero on the left side as a specular reflection of the spin is assumed on the graphene edges. Since the reference electrode closest to the injector is also FM, it acts as a second spin source ($\downarrow\uparrow$ configuration—orange line) or a spin well ($\uparrow\uparrow$ configuration—blue line). Indeed, as the charge-current direction is opposed for both injection contacts, the antiparallel configuration leads to an amplified signal. Regarding the detection, as the tunnel contacts are resistive enough to avoid spin absorption, the spin accumulation μ_s is independent of the magnetic orientations and the positions of electrodes E_3 and E_4. However, the spin-to-charge conversion factor will be positive if the detecting electrode E_3 is parallel to the injecting one and negative if it is antiparallel. This is apparent in Fig. 3(b), which shows the result of a NLSV measurement as a function of the in-plane magnetic field. A sweeping of the in-plane magnetic field $B_{||}$ is applied to change the relative orientation of the electrodes as their coercive field decreases with increasing contact width. The nonlocal resistance R_{NL} can assume four different values depending of the relative orientation of the magnetic moments of the electrodes. Fundamentally, the experimental observation of more than two values for R_{NL} is sufficient proof that external electrodes are perturbing the system, whereas some uncertainty remains with the observation of only two values of R_{NL} [45].
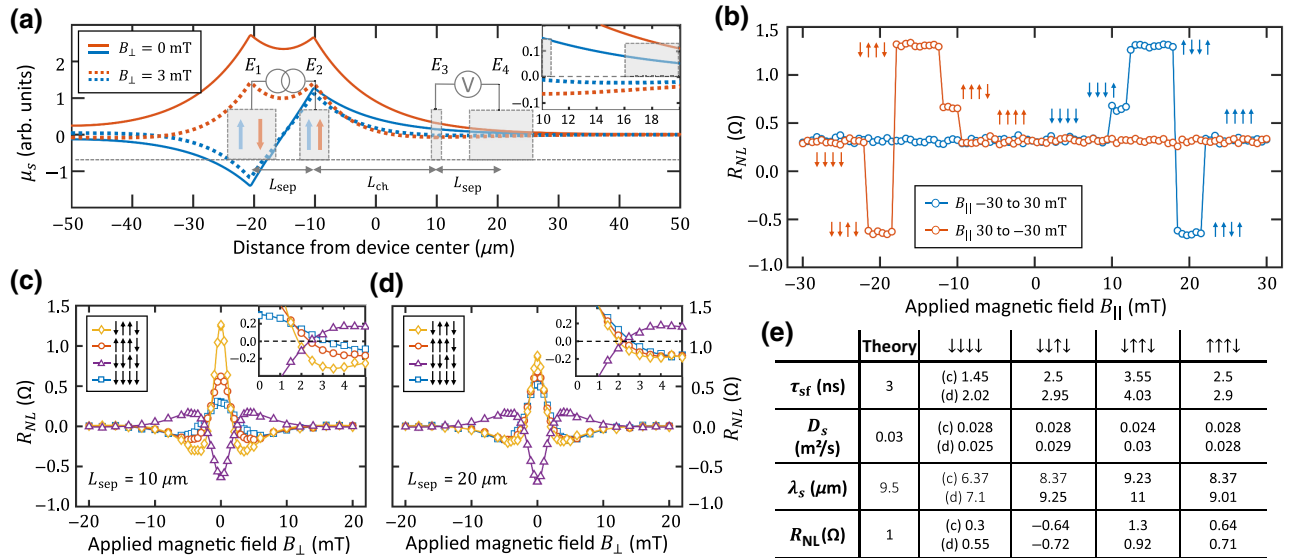

FIG. 3. Effect of the magnetic orientation and position of the outer electrodes on the spin FOMs obtained in Hanle precession experiments. (a) Schematic plot of the spin accumulation μ_s with the position in the device for two opposite directions of the injector magnetization (blue and orange curves) and two external $B_\perp$ values (solid and dashed lines). $\uparrow$ and $\downarrow$ refer to the in-plane orientation. The inset shows an enlargement of the region between E_3 and E_4. (b) Nonlocal resistance as a function of the in-plane magnetic field in a range covering all possible magnetic moment configurations. (c), (d) Hanle spin-precession simulations for a separation distance L_{sep} of (c) 10 μm and (d) 20 μm. Solid lines are fitting curves, while symbols are simulated data. The insets show englargements of the $B_\perp$ range for which the spin signal crosses the zero value. (e) Extracted FOMs from the Hanle curves in (c),(d). Simulations in (a)–(d) are achieved by our using spin FOMs reported in Ref. [6] and parameters detailed in Appendix A as input parameters.

A. Effect of L_{sep} variation

We focus now on the effect of a spin Hanle experiment ($B_\perp \neq 0$). The FOMs cannot be extracted by fitting Hanle spin-precession data with the solution of the modified Bloch equation. Indeed, as shown in Fig. 3(c), the shape of the Hanle curve depends on the magnetization orientation. In particular, the spin signal vanishes at different values of $B_\perp$ depending on the magnetic configuration of the electrodes. This effect is less pronounced if the distance between inner and outer electrodes increases, as shown in Fig. 3(d). To understand the origin of the change in the spin Hanle curve, the calculated spin-accumulation profile in presence of a perpendicular magnetic field $B_\perp = 3$ mT (for which the Hanle signal is close to zero in the $\uparrow\uparrow\uparrow\uparrow$ configuration) is displayed in Fig. 3(a) (dashed lines). Under a perpendicular magnetic field, spins diffusing from the injector have a shorter coherence length as $B_\perp$ forces the precession of spins. It results notably in a zero-accumulation point at a specific distance from the injector (see the inset for an enlargement of the region between the detector and the reference electrode). This position is fully determined by the spin-transport properties of the channel and the external magnetic field, and should lead to a root in the Hanle function when the specific position equals the channel length. However, as shown in Fig. 3(c), this root varies from one configuration of FM electrodes to the other, as the zero-accumulation situation is obtained when $\mu_s(E_3) \pm \mu_s(E_4) = 0$, with "±" standing for parallel or antiparallel configurations between E_3 and E_4, respectively. Such a deviation of the experimental data results in inaccuracy for the estimation of τ_{sf} and D_s when the classical Hanle model is used as a fit function. The extracted data are well fitted by the Hanle function in Figs. 3(c) and 3(d). However, as shown in Fig. 3(e), the measured spin FOMs from Figs. 3(c) and 3((d) depart from the theoretical values used as input for the calculations. The diffusion length is underestimated whatever the magnetic configuration, except for the configuration ($\downarrow\uparrow\uparrow\downarrow$) with $L_{\mathrm{sep}} = 20$ μm. In this particular magnetic configuration of electrodes, the probed spin signal is maximum and the spin lifetime is overestimated for both values of L_{sep}. In contrast, the detected signal is strongly reduced (less than a third of the theoretical value) when the most-common configuration ($\downarrow\downarrow\downarrow\downarrow$) is used, as both spin sources act oppositely and because the detected voltage is the electrical potential difference between E_3 and E_4 in the parallel configuration. The diffusion coefficient is also underestimated but, as shown in Fig. 4 (see the discussion below), all these results depend strongly and nonmonotonically on the separation distance. It is also shown that the $\downarrow\uparrow\uparrow\uparrow$ and $\uparrow\uparrow\uparrow\downarrow$ configurations lead to equivalent spin FOMs even though the spin-accumulation profile is different (the small difference is due to artificial measurement noise added to the curve). Indeed, as the key parameters are the

four distances between injection and detection electrodes (between E_1 and E_3, between E_1 and E_4, between E_2 and E_3, and between E_2 and E_4), those two specific configurations probe the same signal as long as the separation distance is the same for the injection part and the detection part of the device (i.e., the distance between E_1 and E_3 is identical to the distance between E_2 and E_4). The above observations highlight the importance of including the effect of the outer electrodes when the fifth hypothesis is not fulfilled and therefore when the distance between E_2 and E_3 is no longer the only relevant quantity.

In Fig. 4, the influence of the separation distance at the detector (L_2) is studied for a fixed separation distance at the injector L_1 (in Fig. 3, $L_1 = L_2 = L_{\mathrm{sep}}$). The channel length is set to 20 μm. For symmetry reasons, a variation of L_1 with fixed L_2 leads to the same conclusion. Calculations are performed assuming a spin lifetime of 3.2 ns and a spin diffusion coefficient of 200 cm^2/s, which are typical reported values for graphene-based spin experiments [6]. The horizontal dashed lines represent the theoretical values. The results displayed in Figs. 4(a) and 4(c) are obtained by our using $L_1 = 10$ μm, while for Figs. 4(b) and 4(d), $L_1 = 60$ μm is used. Careful inspection of Fig. 4 leads us to several observations. Firstly, both the spin lifetime τ_{sf} and the spin diffusion coefficient D_s are incorrectly evaluated, and the variation of the inaccuracy with the separation distance is not monotonic for each configuration.
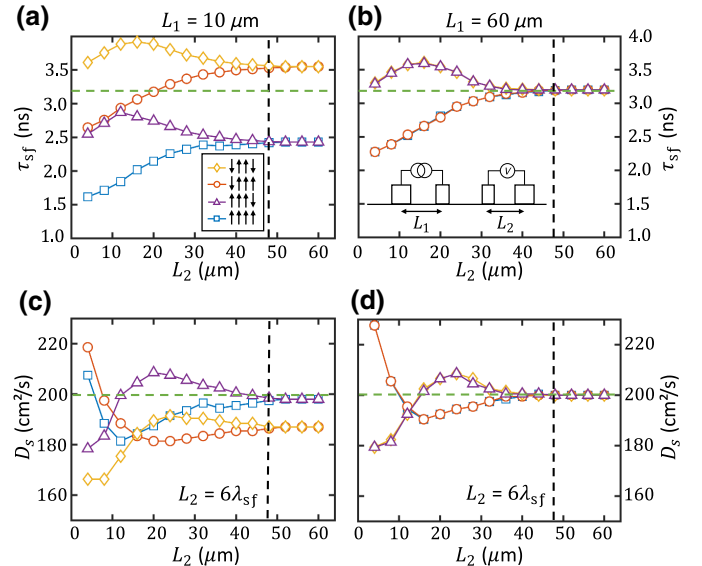

FIG. 4. Effect of the separation distance L_2 between the detector and the closest outer electrode for four different relative magnetizations of the electrodes. (a),(b) The extracted spin lifetime τ_{sf} as a function of L_2 for $L_1 = 10$ μm and $L_1 = 60$ μm, respectively. (c), (d) Variation of the spin diffusion coefficient D_s under similar conditions. The horizontal dashed green lines refer to the theoretical value of D_s and τ_{sf}. The vertical dashed black lines serve as markers for $L_2 = 6\lambda_{\mathrm{sf}}$.

Secondly, the magnitude of the associated error depends strongly on the polarization of the FM electrodes, which confirms the observation above that the most- widely-used configuration ($\uparrow\uparrow\uparrow\uparrow$) leads to the largest error for the spin diffusion length. Thirdly, FOM values do converge toward a common reference when the separation distance is larger than nearly $6\lambda_{sf}$, which is therefore considered as the minimal separation distance to ensure a correct fit. As shown in Fig. 2(b), this criterion is rarely met in the literature. There are two asymptotic values for the data in Figs. 4(a) and 4(c), one for each relative polarization of the FM electrode with a separation distance fixed at 10 μm. When both separation distances are large enough, τ_{sf} and D_s are correctly extracted with use of the basic form of the fit function.

B. Impact of error variation on data interpretation

The two main candidates to explain spin relaxation in graphene are the Elliot-Yafet mechanism and the D'yakonov-Perel mechanism [2]. Theoretically, the first one is characterized by a linear relation between the spin and the quasimomentum relaxation times $\tau_p \propto \tau_{sf}$, while the second one follows the inverse relation $\tau_p \propto \tau_{sf}^{-1}$. Currently the determination of the dominant spin-relaxation mechanisms remains puzzling. For a NLSV, a common method to distinguish the main relaxation source consists in the evaluation of the reciprocal change in the spin lifetime and diffusion coefficient with an external parameter such as the temperature or the charge-carrier concentration (via a gate voltage) [36,46]. However, in the presence of four magnetic electrodes with limited L_{sep}, the relation between D_s and τ_{sf} will deviate from the intrinsic behavior due to a change in the FOM extraction error. To illustrate this effect, simulations are performed to map the error when the spin FOMs vary. Values for the $\uparrow\uparrow\uparrow\uparrow$ configuration with electrodes separated by 10 μm from each other are shown in Fig. 5.Figs. 5(a) and 5(b) show the relative error $(K_{\text{probed}} - K_{\text{theor}})/K_{\text{theor}}$ for $K = D_s$ and $K = \tau_{sf}$, respectively. While the error evolves similarly in Figs. 5(a) and 5(b) (negative with τ_{sf} or D_s increase), it is significantly more pronounced for the spin lifetime.

These observations have two consequences for experimental reports as presented in Figs. 5(c) and 5(d). First, there may be a clear misleading dependence of the spin FOMs on the external parameters. For example, the spin diffusion coefficient is theoretically expected to evolve as $D_s \propto \sqrt{n}$, and the same trend is generally observed for τ_{sf} [4,6,8]. Therefore, for a device with a short distance between outer and inner electrodes, the extraction error increases when the carrier concentration is experimentally increased to study the change of D_s and τ_{sf}. As a result, experiments will lead to the conclusion of a variation of spin FOMs different from that expected theoretically, such
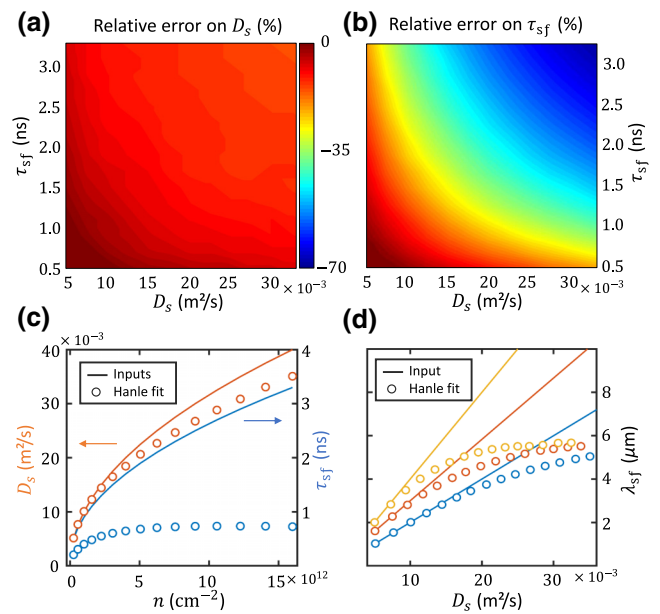

FIG. 5. Evolution of the relative error (a) on the spin diffusion constant and (b) on the spin lifetime when the classical Hanle fit curve is used as a function of τ_{sf} and D_s. (c) Example of deviation of extracted FOMs in the carrier-density-variation experiment. (d) Correlation between λ_{sf} and D_s at different carrier densities. Solid lines are theoretical (exact) values and circles are extracted values obtained with the Hanle fit function. Different colors represent different experimental setups (different temperatures or substrates, for example).

as a spin lifetime independent of or decreasing with the carrier concentration [6].

As an example, we simulate the deviation from a theoretical $\sqrt{n}$ variation. The results are presented in Fig. 5(c). Obviously, similar effects are expected when a temperature variation is considered since it will influence the quasi-momentum scattering time and therefore the spin lifetime [1,39]. Moreover, as the relative error is more pronounced for the spin lifetime, outer electrodes may also lead to incorrect conclusions on the spin-relaxation mechanism. As observed in Fig. 5(d), a departure from the linear relationship between λ_{sf} and D_s might be attributed to a change of relaxation mechanism, while it actually due to the proximity of the outer electrodes. Since the question of the dominant spin-relaxation mechanism is still open, it is important to avoid any source of confusion, including the often-overlooked impact of the outer electrodes, which could lead to misinterpretation of results. In the following section, we provide clear guidelines for the design of a four-terminal NLSV capable of yielding flawless estimations of the spin lifetime and the spin diffusion coefficient without increasing the complexity of the fabrication process.

III. METHOD FOR ACCURATE EXTRACTION OF SPIN FIGURES OF MERIT

To correctly extract the spin diffusion length, we propose three methods, each of them with pros and cons. A first way is purely based on the fabrication process. The spin-valve device is designed in such a way that the outer electrodes do not influence the Hanle curve. This can be achieved by ensuring that the distance between the FM inner and outer electrodes is large enough ($L_{sep} > 6\lambda_{sf}$ leads to less than 1% inaccuracy) or by use of nonmagnetic tunnel outer electrodes. The obvious downside of this approach is the requirement of larger devices for the former or more-involved nanofabrication processing for the latter (such as a shadow evaporation process [8] or a double-lithography process [16]). An alternative method consists in performing the Hanle experiment in all four different configurations with a positive zero-magnetic field signal ($\uparrow\uparrow\uparrow\uparrow$, $\downarrow\uparrow\uparrow\uparrow$, $\downarrow\uparrow\uparrow\downarrow$, and $\uparrow\uparrow\uparrow\downarrow$) and applying the classical fit method on the mean of those measurements [47]. However, this approach needs specific widths or shapes to obtain a different coercive field for each FM electrode. This method is somehow limited by the fact that it is challenging to ensure an optimal spin injection or detection at each electrode when they are not magnetized at saturation.

The third method consists in magnetizing all electrodes at saturation along the same direction and fitting the data with a modified version of Eq. (24) in Ref. [10]. The new fit function sums the contributions of the four injector-detector couples in a full FM spin valve:

$$R_{nl} = \frac{V_{spin}}{I} = \frac{\pi \hbar^2 v_0^2}{g_s g_v \tilde{\mu}} \frac{P^2}{e^2 W} \sqrt{\frac{\tau_{sf}}{2D_s}} [F(L_{ch}, B_\perp)$$
$$- F(L_1 + L_{ch}, B_\perp) - F(L_2 + L_{ch}, B_\perp)$$
$$+ F(L_1 + L_2 + L_{ch}, B_\perp)], \qquad (1)$$

where e is the electron charge, $\tilde{\mu}$ is the mean electrochemical potential (Appendix B 1), and W is the channel width. The function $F(L, B)$ is developed in Appendix B 2. The major advantage of this approach is that there is no fabrication constraint on the device, and therefore more than four electrodes can be fabricated on one graphene ribbon or flake (for multiple NLSVs with different channel lengths as shown in Fig. 1). It also allows one to work with short separation distances and therefore to drastically reduce the thermal noise. However, as shown in the table in Fig. 3(e), the nonlocal resistance is weaker when the $\uparrow\uparrow\uparrow\uparrow$ configuration is used. In case of NM tunnel contacts for the outer

electrodes (see Ref. [8]), Eq. (1) can be considerably simplified since only $F(L_{ch}, B_\perp)$ is nonzero. Additionally, a solution dealing with NM metallic outer electrodes and FM tunnel inner electrodes does exist [24] and has to be used for devices such as those proposed in the references with an asterisk in Fig. 2(a). Vila *et al.* [24] assumed that no spin-sink effect occurs at both the injector and the detector due to the presence of a pinhole-free tunnel barrier. This hypothesis also holds for Eq. (1) as claimed by authors of recent experimental publications [6,8,48–50]. Moreover, the application of our method does not require electrodes with different widths. Therefore, using only very narrow electrodes, this approach respects or bypasses all hypotheses of Hanle precession equations presented in Sec. I, except for the condition related to an infinite diffusive medium.

IV. CONCLUSION

In summary, we demonstrate that the distance between inner and outer electrodes of a spin-valve device strongly influences the value of extracted spin FOMs when a Hanle precession method is used. Our calculations reveal that a separation distance $L_{sep} > 6\lambda_{sf}$ is mandatory to avoid the influence of outer electrodes. As this criterion has been hardly met in previous experimental reports, we anticipate that some conclusions concerning the benefits of particular fabrication processes or material choices might need to be revisited in the light of this work. Finally, we demonstrate that working with spin-valve devices with four identical thin ferromagnetic tunnel contacts and a short distance between inner and outer electrodes will simplify the fabrication processes and reduce the experimental noise, while still providing accurate FOMs if a modified version of the Hanle fit equation [Eq. (1)] is used.

APPENDIX A: COMPUTATIONAL DETAILS

Simulations are performed by our using the finite-element-method commercial software program COMSOL MULTIPHYSICS with a geometry based on the cross section of the device presented in Fig. 1. The charge-current distribution is calculated via the electrical current module, while spin drift-diffusion equations are manually included for the

three spin directions:

$$eD_s \begin{pmatrix} \nabla^2 n_{s,x} \\ \nabla^2 n_{s,y} \\ \nabla^2 n_{s,z} \end{pmatrix} + e\mu_n \begin{pmatrix} n_{s,x} \\ n_{s,y} \\ n_{s,z} \end{pmatrix} \nabla V - \frac{g\mu_B}{\hbar} \begin{pmatrix} n_{s,x} \\ n_{s,y} \\ n_{s,z} \end{pmatrix}$$
$$\times \begin{pmatrix} B_x \\ B_y \\ B_z \end{pmatrix} = \frac{e}{\tau_{sf}} \begin{pmatrix} n_{s,x} \\ n_{s,y} \\ n_{s,z} \end{pmatrix}. \qquad (A1)$$

A zero-flux boundary condition is used at the edge of the graphene and the ribbon. The charge current is fixed at electrode E_2, while electrode E_1 is grounded and electrodes E_2 and E_3 are floating. Simulations are performed with the following parameters under the assumption that the charge and spin diffusion coefficients are equal: charge current at the injector $I = 5~\mu A$, tunnel contact resistivity $\rho_c = 10^{-8}~\Omega m^2$ (no spin absorption is expected), carrier density $n = 3.6 \times 10^{12}~cm^{-2}$, carrier mobility $\mu_n = eD_s/k_BT$, spin polarization $P = 10\%$, and graphene-ribbon width $w = 5~\mu m$ and length $L = 200~\mu m$ (impact of spin-carrier reflection at the ribbon edges is negligible).

APPENDIX B: NONLOCAL-RESISTANCE-FORMULA DETAILS

1. From n_s to V_{spin}

The spin voltage $V_{spin} = \frac{P}{2}e\mu_s$ is deduced from the spin-dependent carrier concentration in the graphene sheet by integration of the product of the density of states by the Fermi-Dirac distribution $f(E - \mu_\pm)$, where $\mu_\pm$ is the spin-dependent electrochemical potential. Assuming n-type conductivity in graphene and integrating from 0 to ∞, one can find the following solution with a second-order logarithm integral [51]:

$$n_\pm = \frac{1}{2} \int_0^\infty \nu(E) f(E - \mu_\pm) dE$$
$$= -\frac{1}{\pi} \left(\frac{k_BT}{\hbar v_0} \right)^2 Li_2 \left(-e^{\mu_\pm/k_BT} \right). \qquad (B1)$$

Assuming that $\mu_s = \mu_+ - \mu_- \ll \tilde{\mu} = \mu_+ + \mu_-$ and with the Taylor second-order approximation, we obtain the following linear relation between the spin concentration n_s and the spin accumulation μ_s in the case of moderate carrier concentration ($\mu_\pm < 5k_BT$):

$$n_s = n_+ - n_- \simeq \frac{g_s g_v}{4\pi \hbar^2 v_0^2} \left[\frac{\ln(2)}{2} k_BT + \tilde{\mu} \right] \mu_s \qquad (B2)$$

For high carrier concentration ($\mu \gg k_BT$), we obtain

$$n_s = n_+ - n_- \simeq g_s g_v \frac{\tilde{\mu}}{4\pi \hbar^2 v_0^2} \mu_s. \qquad (B3)$$

Using the same reasoning, we approximate the mean electrochemical potential $\tilde{\mu}$ in terms of the temperature and the total carrier concentration (experimentally measurable values):

$$\tilde{\mu} = k_BT \sqrt{\frac{2\pi}{g_s g_v} \left(\frac{\hbar v_0}{k_BT} \right)^2 n - \frac{\pi}{12}}. \qquad (B4)$$

2. Definition of $F(B, L)$

We define

$$b = \omega_L \tau_{sf} = -\frac{g\mu_B B_\perp}{\hbar} \tau_{sf}, \qquad (B5)$$

$$f(b) = \sqrt{1 + \sqrt{1 + b^2}}, \qquad (B6)$$

$$l = \sqrt{\frac{L^2}{2\tau_{sf} D_s}}, \qquad (B7)$$

where ω_L is the Larmor frequency, g is the gyroscopic factor, μ_B is the Bohr magneton, and $\hbar$ is Planck's constant.

$$F(b, l) = \frac{1}{f^2(b) - 1}$$
$$\times \left[f(b) \cos \left(\frac{lb}{f(b)} \right) - \frac{b}{f(b)} \sin \left(\frac{lb}{f(b)} \right) \right]$$
$$\times \exp \left(-lf(b) \right). \qquad (B8)$$

APPENDIX C: SPIN-FOM CORRECTION—PRACTICAL CASE

To illustrate why it is important to account for the outer electrodes, we apply our observation on data reported in Ref. [6], for which geometrical details and the magnetic orientation of the four electrodes are given. We compare the classical fit with the one using Eq. (1); see Fig. 6. The spin lifetime changes from 3 ns with the classical fit to 3.9 ns (increase of 30%). The spin diffusion coefficient changes from 0.030 to 0.031 m^2/s. The difference between both fit curves is not visible to the naked eye, while the change of values for the spin FOMs is not negligible.
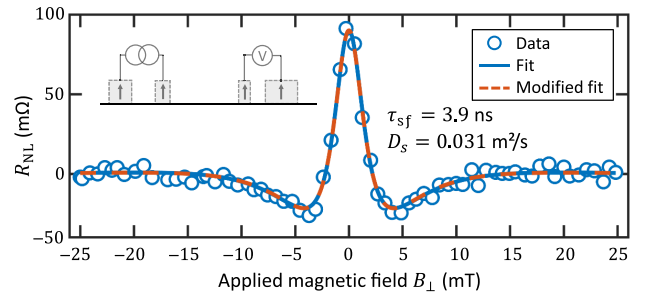

FIG. 6. Correction of the extraction of spin FOMs using Eq. (1) as the fit function. Data are from Ref. [6].

[1] A. Avsar, H. Ochoa, F. Guinea, B. Özyilmaz, B. J. van Wees, and I. J. Vera-Marun, Colloquium: Spintronics in graphene and other two-dimensional materials, Rev. Mod. Phys. **92,** 21003 (2020).

[2] W. Han, R. K. Kawakami, M. Gmitra, and J. Fabian, Graphene spintronics, Nat. Nanotechnol. **9,** 794 (2014).

[3] M. H. D. Guimarães, P. J. Zomer, J. C. Brant, N. Tombros, and B. J. V. Wees, Controlling Spin Relaxation in Hexagonal BN-Encapsulated Graphene with a Transverse Electric Field, Phys. Rev. Lett. **113,** 086602 (2014).

[4] M. Drögeler, C. Franzen, F. Volmer, T. Pohlmann, L. Banszerus, M. Wolter, K. Watanabe, T. Taniguchi, C. Stampfer, and B. Beschoten, Spin lifetimes exceeding 12 ns in graphene nonlocal spin valve devices, Nano Lett. **16,** 3533 (2016).

[5] J. Ingla-Aynés, R. J. Meijerink, and B. J. V. Wees, Eighty-eight percent directional guiding of spin currents with 90 μm relaxation length in bilayer graphene using carrier drift, Nano Lett. **16,** 4825 (2016).

[6] Z. M. Gebeyehu, S. Parui, J. F. Sierra, M. Timmermans, M. J. Esplandiu, S. Brems, C. Huyghebaert, K. Garello, M. V. Costache, and S. O. Valenzuela, Spin communication over 30 μm long channels of chemical vapor deposited graphene on SiO_2, 2D Mater. **6,** 034003 (2019).

[7] D. Huertas-Hernando, F. Guinea, and A. Brataas, Spin-Orbit-Mediated Spin Relaxation in Graphene, Phys. Rev. Lett. **103,** 146801 (2009).

[8] B. Raes, J. E. Scheerder, M. V. Costache, F. Bonell, J. F. Sierra, J. Cuppens, J. Van De Vondel, and S. O. Valenzuela, Determination of the spin-lifetime anisotropy in graphene using oblique spin precession, Nat. Commun. **7,** 1 (2016).

[9] B. Raes, A. W. Cummings, F. Bonell, M. V. Costache, J. F. Sierra, S. Roche, and S. O. Valenzuela, Spin precession in anisotropic media, Phys. Rev. B **95,** 085403 (2017).

[10] M. Johnson and R. H. Silsbee, Coupling of electronic charge and spin at a ferromagnetic-paramagnetic metal interface, Phys. Rev. B **37,** 5312 (1988).

[11] X. Lou, C. Adelmann, S. A. Crooker, E. S. Garlid, J. Zhang, K. S. M. Reddy, S. D. Flexner, C. J. Palmstrøm, and P. A. Crowell, Electrical detection of spin transport in lateral ferromagnet–semiconductor devices, Nat. Phys. **3,** 197 (2007).

[12] F. Volmer, M. Drögeler, E. Maynicke, N. von den Driesch, M. L. Boschen, G. Güntherodt, and B. Beschoten, Role of MgO barriers for spin and charge transport in Co/MgO/graphene nonlocal spin-valve devices, Phys. Rev. B **88,** 161405 (2013).

[13] E. Sosenko, H. Wei, and V. Aji, Effect of contacts on spin lifetime measurements in graphene, Phys. Rev. B **89,** 245436 (2014).

[14] F. Volmer, M. Drögeler, T. Pohlmann, G. Güntherodt, and C. Stampfer, Contact-induced charge contributions to non-local spin transport measurements in Co/MgO/graphene devices, 2D Mater. **2,** 024001 (2015).

[15] M. V. Kamalakar, A. Dankert, P. J. Kelly, and S. P. Dash, Inversion of spin signal and spin filtering in ferromagnet — hexagonal boron nitride-graphene van der Waals heterostructures, Sci. Rep. **6,** 21168 (2016).

[16] G. Stecklein, P. A. Crowell, J. Li, Y. Anugrah, Q. Su, and S. J. Koester, Contact-Induced Spin Relaxation in Graphene Nonlocal Spin Valves, Phys. Rev. Appl. **6,** 054015 (2016).

[17] W. Amamou, Z. Lin, J. V. Baren, S. Turkyilmaz, J. Shi, and R. K. Kawakami, Contact induced spin relaxation in graphene spin valves with Al_2O_3 and MgO tunnel barriers, APL Mater. **4,** 032503 (2016).

[18] T. Maassen, I. J. Vera-Marun, M. H. D. Guimar, and B. J. van Wees, Contact-induced spin relaxation in hanle spin precession measurements, Phys. Rev. B **86,** 235408 (2012).

[19] H. Idzuchi, A. Fert, and Y. Otani, Revisiting the measurement of the spin relaxation time in graphene-based devices, Phys. Rev. B **91,** 241407 (2015).

[20] M. Gurram, S. Omar, and B. J. V. Wees, Bias induced up to 100% spin-injection and detection polarizations in ferromagnet/bilayer-hBN/graphene/hBN heterostructures, Nat. Commun. **8,** 1 (2017).

[21] E. Fourneau, A. V. Silhanek, and N. D. Nguyen, Origin of the Giant Spin-Detection Efficiency in Tunnel-Barrier-Based Electrical, Phys. Rev. Appl. **14,** 024020 (2020).

[22] M. Wojtaszek, I. J. Vera-Marun, and B. J. van Wees, Transition between one-dimensional and zero-dimensional spin transport studied by Hanle precession, Phys. Rev. B **89,** 245427 (2014).

[23] M. Drögeler, F. Volmer, C. Stampfer, and B. Beschoten, Simulations on the influence of spatially varying spin transport parameters on the measured spin lifetime in graphene non-local spin valves, Phys. Status Solidi (B) **254,** 1700293 (2017).

[24] M. Vila, J. H. Garcia, A. W. Cummings, S. R. Power, C. W. Groth, X. Waintal, and S. Roche, Nonlocal Spin Dynamics in the Crossover from Diffusive to Ballistic Transport, Phys. Rev. Lett. **124,** 196602 (2020).

[25] A. Spiesser, H. Saito, Y. Fujita, S. Yamada, K. Hamaya, S. Yuasa, and R. Jansen, Giant Spin Accumulation in Silicon Nonlocal Spin-Transport Devices, Phys. Rev. Appl. **8,** 1 (2017).

[26] Spiesser *et al.* experimentally test the correction factor in four-terminal devices with a highly doped silicon channel. This is acceptable under the hypothesis of a homogeneous current-density distribution along the contact width. In two-dimensional materials, a substantial current-crowding effect at the injector implies highly inhomogeneous current distributions unless the tunnel barrier is resistive enough, which is indeed the case for most of the two-dimensional-material spin-valve devices reported in the literature.

[27] N. Tombros, C. Jozsa, M. Popinciuc, H. T. Jonkman, and B. J. V. Wees, Electronic spin transport and spin precession in single graphene layers at room temperature, Nature **448,** 571 (2007).

[28] C. Jozsa, M. Popinciuc, N. Tombros, H. T. Jonkman, B. J. V. Wees, and C. Jo, Electronic Spin Drift in Graphene Field-Effect Transistors, Phys. Rev. Lett. **100,** 236603 (2008).

[29] W. Han, K. Pi, K. M. Mccreary, Y. Li, J. J. I. Wong, A. G. Swartz, and R. K. Kawakami, Tunneling Spin Injection Into Single Layer Graphene, Phys. Rev. Lett. **105,** 167202 (2010).

[30] W. Han, K. M. Mccreary, K. Pi, W. H. Wang, Y. Li, H. Wen, J. R. Chen, and R. K. Kawakami, Spin transport and relaxation in graphene, J. Magn. Magn. Mater. **324,** 369 (2012).

[31] I. Neumann, M. V. Costache, G. Bridoux, J. F. Sierra, and S. O. Valenzuela, Enhanced spin accumulation at room temperature in graphene spin valves with amorphous

carbon interfacial layers, Appl. Phys. Lett. **112401,** 112401 (2013).

[32] A. J. Berger, M. R. Page, H. Wen, K. M. Mccreary, V. P. Bhallamudi, K. Roland, and P. C. Hammel, Correlating spin transport and electrode magnetization in a graphene spin valve: Simultaneous magnetic microscopy and non-local measurements, Appl. Phys. Lett. **107,** 142406 (2015).

[33] M. H. D. Guimarães, J. J. van den Berg, I. J. Vera-Marun, P. J. Zomer, and B. J. van Wees, Spin transport in graphene nanostructures, Phys. Rev. B **90,** 235428 (2014).

[34] N. Tombros, S. Tanabe, A. Veligura, C. Jozsa, M. Popinciuc, H. T. Jonkman, and B. J. V. Wees, Anisotropic Spin Relaxation in Graphene, Phys. Rev. Lett. **101,** 046601 (2008).

[35] M. Popinciuc, C. Józsa, P. J. Zomer, N. Tombros, A. Veligura, H. T. Jonkman, and B. J. V. Wees, Electronic spin transport in graphene field-effect transistors, Phys. Rev. B **80,** 214427 (2009).

[36] C. Józsa, M. Popinciuc, N. Tombros, H. T. Jonkman, and B. J. V. Wees, Controlling the efficiency of spin injection into graphene by carrier drift, Phys. Rev. B **79,** 081402(R) (2009).

[37] M. H. D. Guimarães, A. Veligura, P. J. Zomer, T. Maassen, N. Tombros, and B. J. V. Wees, Spin transport in high-quality suspended graphene devices, Nano Lett. **12,** 3512 (2012).

[38] P. J. Zomer, M. H. D. Guimarães, N. Tombros, and B. J. van Wees, Long-distance spin transport in high-mobility graphene on hexagonal boron nitride, Phys. Rev. B. **86,** 161416(R) (2012).

[39] M. V. Kamalakar, C. Groenveld, A. Dankert, and S. P. Dash, Long distance spin communication in chemical vapour deposited graphene, Nat. Commun. **6,** 1 (2015).

[40] W. S. Torres, J. F. Sierra, L. A. Benítez, F. Bonell, M. V. Costache, and S. O. Valenzuela, Spin precession and spin Hall effect in monolayer graphene/Pt nanostructures, 2D Mater. **4,** 041008 (2017).

[41] M. V. Kamalakar, J. Bergsten, T. Ive, and S. P. Dash, Enhanced tunnel spin injection into graphene using chemical vapor deposited hexagonal boron nitride, Sci. Rep. **4,** 6146 (2014).

[42] S. Singh, J. Katoch, T. Zhu, R. J. Wu, A. S. Ahmed, W. Amamou, D. Wang, K. A. Mkhoyan, and R. K. Kawakami, Strontium oxide tunnel barriers for high quality spin transport and large spin accumulation in graphene, Nano Lett. **17,** 7578 (2017).

[43] A. L. Friedman, C. H. Li, J. T. Robinson, and B. T. Jonker, Homoepitaxial tunnel barriers with functionalized graphene-on-graphene for charge and spin transport, Nat. Commun. **5,** 3161 (2014).

[44] I. Žutíc, J. Fabian, and S. D. Sarma, Spintronics: Fundamentals and applications, Rev. Mod. Phys. **76,** 323 (2004).

[45] The absence of more than two values for R_{NL} in spin-valve measurements implies that external electrodes have no impact only if one can prove that all configurations have been probed. For example, only two values for R_{NL} will be observed if the external electrodes are narrow enough to sustain a large in-plane magnetic field or if each outer electrode has a coercive field similar to that of the closest inner electrode [$B_c(E_1) \simeq B_c(E_2)$ and $B_c(E_3) \simeq B_c(E_4)$].

[46] T. Maassen, F. K. Dejene, M. H. D. Guimarães, C. Jozsa, and B. J. van Wees, Comparison between charge and spin transport in few-layer graphene, Phys. Rev. B **83,** 115410 (2011).

[47] Using the four variations ↑↑↑↑, ↓↑↑↑, ↓↑↑↓, and ↑↑↑↓, we maintain the orientation of inner electrodes (E_2 and E_3) and take the four different configurations for the outer electrodes (E_1 and E_4). As a result, in half of the configurations E_1 injects spin (↓↑↑↑ and ↓↑↑↓), while it absorbs for the two other configurations, leading to spin signal generated with an opposite sign. The same reasoning is used for the sign of the spin voltage detected in E_4. Therefore, only the spin signal generated at E_2 and detected at E_3 remains after calculation of the mean of the four signals. The sign of each term in Eq. (1) corresponds to the relative orientation of the two electrodes involved. Thereby, after application of the mean to Eq. (1), only $F(B_\perp, L_{ch})$ remains.

[48] J. C. Leutenantsmeyer, J. Ingla-Aynés, M. Gurram, and Bart J. van Wees, Efficient spin injection into graphene through trilayer hBN tunnel barriers, J. Appl. Phys. **124,** 194301 (2018).

[49] J. Panda, M. Ramu, O. Karis, T. Sarkar, and M. V. Kamalakar, Ultimate Spin Currents in Commercial Chemical Vapor Deposited Graphene, ACS Nano **14,** 12771 (2020).

[50] S. Chen, R. Ruiterand, V. Mathkar, B. J. Van Wees, and T. Banerjee, Temperature and electric field dependence of spin relaxation in graphene on SrTiO₃, Phys. Status Solidi RRL **12,** 1800216 (2018).

[51] G. Zebrev, in Physics and Applications of Graphene – Theory, edited by S. Mikhailov (InTech, Croatia, 2011), p. 475.